AGU PUBLICATIONS

JGR

Journal of Geophysical Research: Oceans

RESEARCH ARTICLE

10.1002/2016JC012078

Key Points:

- The temperature and momentum changes in the SCS are decomposed numerically
- A sandwich structure of air-sea coupling relationship is revealed in the SCS
- The WES mechanism plays an important role on the temperature warming trend in the SCS

Correspondence to:
J. Wei,
junwei@pku.edu.cn

Citation:
Wei, J., P. Malanotte-Rizzoli, M.-T. Li, and H. Wang (2016), Decomposition of thermal and dynamic changes in the South China Sea induced by boundary forcing and surface fluxes during 1970–2000, *J. Geophys. Res. Oceans*, *121*, doi:10.1002/2016JC012078.

Received 21 JUN 2016
Accepted 5 OCT 2016
Accepted article online 7 OCT 2016

Decomposition of thermal and dynamic changes in the South China Sea induced by boundary forcing and surface fluxes during 1970–2000

Jun Wei[1,2], Paola Malanotte-Rizzoli[3], Ming-Ting Li[1], and Hao Wang[4]

[1]Laboratory for Climate and Ocean-Atmosphere Studies, Department of Atmospheric and Oceanic Sciences, Peking University, Beijing, China, [2]State Key Laboratory of Severe Weather, Chinese Academy of Meteorological Sciences, Beijing, China, [3]Department of Earth, Atmosphere and Planetary Sciences, Massachusetts Institute of Technology, Boston, Massachusetts, USA, [4]Center for Landscape and Climate Research, University of Leicester, Leicester, UK

Abstract Based on a fully coupled, high-resolution regional climate model, this study analyzed three-dimensional temperature and momentum changes in the South China Sea (SCS) from 1970 to 2000, during which period the climate shifts from a decadal La Niña-like condition (before 1976/1977) to a decadal El Niño-like condition afterward. With a set of partially coupled experiments, sea surface temperature (SST) and kinetic energy (KE) changes during this period are first decomposed into two components: those induced by lateral boundary forcing and those induced by atmospheric surface fluxes. The results showed that the total SST and KE changes show an increasing trend from 1970 to 2000. The two decomposed components together determined 96 and 89% of the SST and KE changes, respectively, implying their dominant roles on the SCS's surface variability. Spatially, a sandwich pattern of air-sea forcing relationship is revealed in the SCS basin. The increased KE, represented by a cyclonic flow anomaly in the northern SCS, was induced by enhanced cold water intrusion from Pacific into the SCS via the Luzon Strait (boundary forcing). This cold-water inflow, however, resulted in SST cooling along the northern shelf of the SCS. The maximal SST warming occurred in the central SCS and was attributed to the wind-evaporation-SST (WES) positive feedback (surface forcing), in which a southwestward wind anomaly is initialized by SST gradients between the northern and southern SCS. This wind anomaly decelerates the southwestly summer monsoons and in turn increases the SST gradients. Over the shallow Sunda shelf, which is far from the Luzon Strait, the SST/KE variability appeared to be determined primarily by local air-sea interactions. Furthermore, analyses on subsurface components indicated that the subsurface temperature changes are primarily induced by internal ocean mixing, which becomes significantly important below the thermocline. The enhanced subsurface flow is driven by the Luzon Strait inflow as well, and exits the SCS via the Mindoro-Sibutu passage.

1. Introduction

The South China Sea (SCS) is the largest marginal sea to the southeast of the Asian Continent, spanning from 5°N to 25°N and 100°E to 120°E. The average depth of the SCS is about 1200 m, with a maximum depth of 5500 m. It is bound by a narrow shelf along the coast of southern China and a wide continental shelf (the Sunda shelf) to its southwest (Figure 1a). Geographically, the SCS is a semienclosed ocean basin, with major inflows from the western Pacific via the Luzon Strait with a maximum depth of ~2000 m, and outflows into the Java Sea via the Karimata Strait (~40 m) and into the Sulu Sea via the Mindoro Strait (~600 m). On one hand, isolated from the open oceans, the SCS demonstrates characteristic regional climate variability determined by local air-sea interactions. On the other hand, embedded between tropical Pacific and Indian Oceans and between the Asian and Australian Continents, the SCS climate variability can be significantly influenced by large-scale remote forcings, transferred into the SCS through oceanic and atmospheric bridges [*Klein et al.*, 1999; *Gordon*, 1986].

The SCS's general circulation is primarily driven by winds, first interpreted by *Wyrtki* [1961] as an oceanic response to the local seasonally reversed monsoons. Its barotropic component, also known as the South China Sea throughflow (SCSTF) [*Wang et al.*, 2006a; *Qu et al.*, 2009; *Liu et al.*, 2012], transforms cold and salty

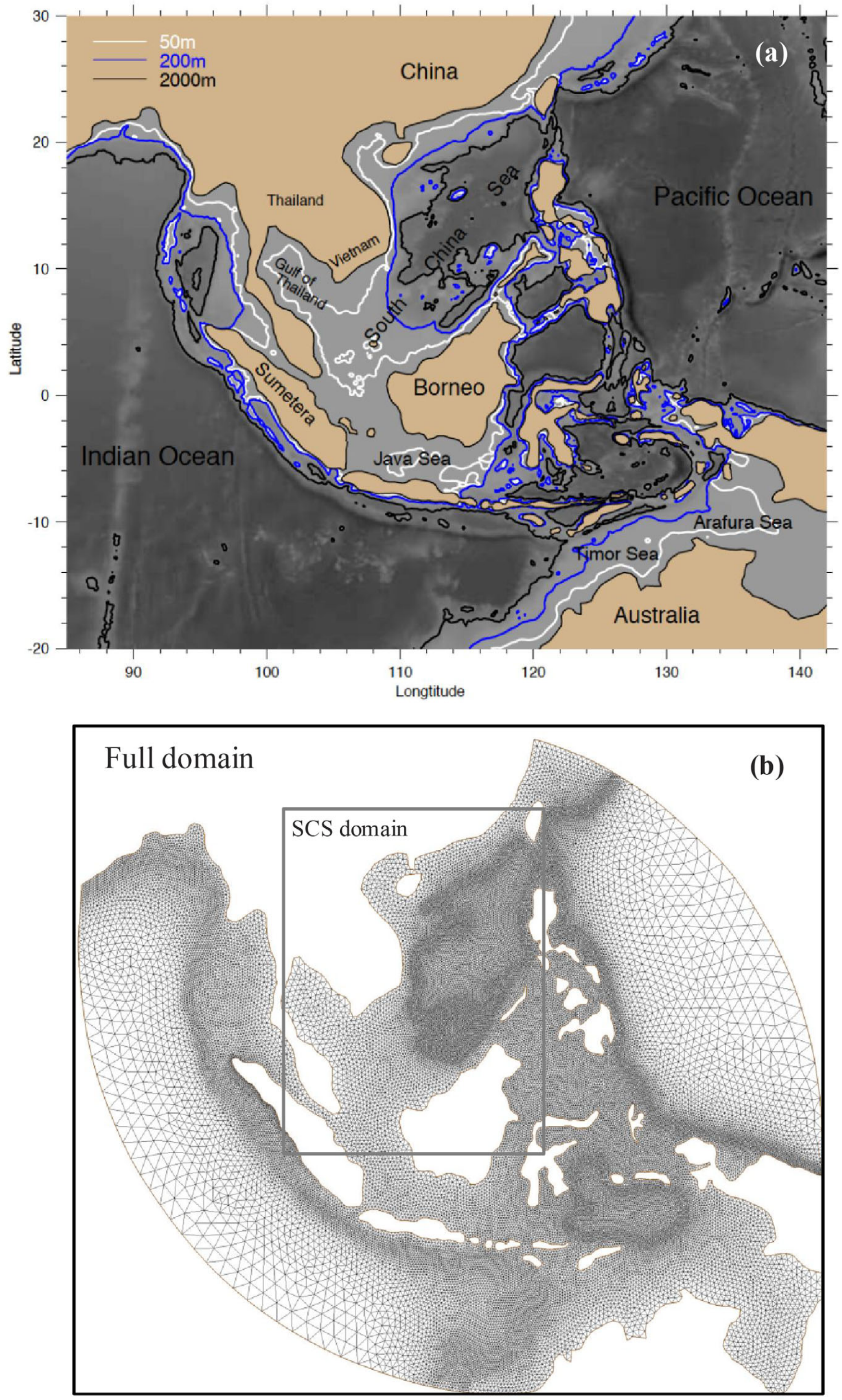

Figure 1. Domains used for (a) RegCM3, with the 50, 200, and 2000 m isobaths and (b) FVCOM, with the unstructured grids (dark gray shading indicates fine triangular grids). The small box in Figure 1b marks the SCS domain for analysis in this study.

water of the western Pacific through the Luzon Strait into the warm and fresh SCS water, outflowing into the Indonesian seas through the Karimata Strait [*Qu*, 2000; *Fang et al*., 2009; *Du and Qu*, 2010; *Xu and Malanotte-Rizzoli*, 2013] and the Mindoro-Sibutu passage [*Metzger and Hurlburt*, 1996; *Gordon et al*., 2012; *Wei et al*., 2016]. A three-layer structure of the SCS basin-wide circulation was simulated by a recent model effort [*Xu and Oey*, 2014] and was related to the sandwich structure of Luzon Strait transports. The variability of sea surface height anomaly (SSHA) of the SCS is attributed to combined effects of wind stress curl and Luzon Strait inflows [*Liu et al*., 2001b; *Xu and Oey*, 2014, 2015; *Cheng et al*., 2015]. On the other hand, the SCS also demonstrates complex thermal structure and variability, from intraseasonal [*Zeng and Wang*, 2009; *Wu*, 2010; *Wei et al*., 2014b] to seasonal [*Liu et al*., 2001a; *Qu*, 2001; *He and Wu*, 2013] and interannual time scales [*Wang et al*., 2006b; *Liu et al*., 2014]. The seasonal SST variability is driven primarily by the local air-sea interactions, for which the seasonal north-south progression of incoming solar radiations and the SCS monsoon winds are the most important forcings [*Chen et al*., 2003a], while the interannual SST variability can be attributed to remote forcings from tropic oceans, such as ENSO variability, transferred into the SCS through the Luzon Strait [*Liu and Xie*, 1999; *Liu et al*., 2001a]. In contrast to the SCS surface variability, its subsurface and intermediate temperature and momentum structures and variability remain less understood [*Chen and Huang*, 1996; *Xu and Oey*, 2014; *Lin et al*., 2016].

According to IPCC reports 2013, a dramatic increase of global mean atmospheric-oceanic surface temperatures has occurred since 1970s, with an accelerated warming period from 1980s to 1990s, and a recent warming hiatus, from 2000 to present [*Meehl et al*., 2011; *Levitus et al*., 2009, 2012; *Abraham et al*., 2013; *Balmaseda et al*., 2013]. The tropical oceans were recognized to play a significantly important role in modulating regional and global climate variability; one interpretation is that the Pacific Decadal Oscillation (PDO) was in a positive phase between 1976 and 1998, corresponding to a warmer Indo-Pacific warm pool [*Trenberth and Fasullo*, 2013], then from 1999, the PDO shifted to a negative phase (and it is still in this phase), producing a colder warm pool [*Lin et al*., 2011]. During a positive (negative) phase of the PDO, the eastern to central tropical Pacific generally becomes warmer (cooler) and the western Pacific becomes cooler (warmer). Another theory considers the interannual ENSO signals [*Easterling and Weher*, 2009; *England et al*., 2014; *Clement and DiNezio*, 2014]; the Niño3.4 index showed that a decadal El Niño-like condition dominated when the PDO was in its positive phase, while La Niña events occurred more frequently before and after this period. Enhanced trade winds in the tropical Pacific and cold SST anomalies in the eastern tropical Pacific during La Niña periods were found to be important forcings in a recent climate model by *Kosaka and Xie* [2013], which largely explains the past 50-year variation of global atmospheric-oceanic surface temperatures.

One of the major challenges in simulating the SCS variability is how to represent accurately the local air-sea interactions and the remote forcings transferred into the SCS, which requires not only a large model domain covering the SCS's surrounding oceans/seas, but also a sufficiently fine resolution to resolves the adjacent island chains and straits. While global reanalysis data sets were commonly used in previous studies, such as SODA, OFES, ECCO2, and HYCOM, their resolutions from 1/2 to 1/10° are often insufficient for those narrow straits ($\sim$40 km) embedded in the Maritime Continent, leading to inconsistent results. By taking advantage of an unstructured grid ocean model, we have developed a fully coupled regional climate model covering the entire Maritime Continent, with a minimal resolution of $\sim$5 km along the shelf break and straits, explicitly resolving the internal throughflows for heat and mass exchanges between the SCS and the adjacent basins and seas. The model also includes large sections of the western Pacific and eastern Indian Oceans, and thus allows remote forcings to transfer into the SCS through the model boundary and surface flux [*Wei et al*., 2014a,2014b].

The climate variability in the SCS is physically complex at multiple time and spatial scales, involving local/remote forcings and natural/anthropogenic effects, which interplay within the SCS. It is rather difficult to separate these processes from each other from observations and reanalysis. On the other hand, from the model point of view, since the temperature and momentum are explicitly integrated using prescribed model surface winds/heat fluxes and boundary forcing, the effects of the surface and boundary forcing can be separated numerically by means of a set of sensitivity experiments. Given the unique geometry of the SCS basin, the surface forcing involves local winds/heat fluxes and those transferred from outside the SCS through the atmospheric bridge. The boundary forcing is generally attributed to the Kuroshio water intrusion through the oceanic passages, e.g., the Luzon Strait. Therefore, the goal of this study is first to decompose numerically the SCS's temperature and momentum changes during a climate transition period (1970–2000) into two components: those induced by ocean boundary forcings and those induced by atmospheric surface fluxes, respectively. We note that although such a decomposition cannot fully decipher the local and remote forcing neither, it provides us insights for better understanding how the remote forcing is transferred into the SCS through the model surface and boundary effects. Second, due to limited observations below surface, the intermediate and deep SCS temperature and momentum variability still remains unclear. By decomposing the surface and subsurface temperature and momentum components, we were able to elucidate both horizontal and vertical extensions of the surface and boundary forcing acting on the SCS basin, which to our best knowledge, has not been achieved by any previous studies. The rest of the paper is organized as follows: section 2 introduces the coupled model used in this study, followed by a detailed description of model configurations and the sensitivity experiments. Section 3 presents the results of temperature and momentum decomposition and the analysis of the individual components. A discussion and concluding remarks are given in section 4.

2. Model and Methods

2.1. A Fully Coupled Regional Climate Model

The coupled climate model used in this study was developed by *Wei et al*. [2014a] for the Maritime Continent, which adopts the Regional Climate Model (RegCM3) as the atmospheric component, the Finite Volume Coastal Ocean Model (FVCOM) as the oceanic one, and OASIS3 as the coupler. RegCM3 was originally developed at the National Center for Atmospheric Research (NCAR) and is now maintained by the International Center for Theoretical Physics (ICTP). The dynamical core of RegCM3 is based on the hydrostatic version of the Pennsylvania State University/NCAR Mesoscale Model Version 5 (MM5) [*Grell et al*., 1994] and employs NCAR's Community Climate Model Version 3 (CCM3) atmospheric radiative transfer scheme (described in *Kiehl et al*. [1996]). FVCOM was originally developed by *Chen et al*. [2003b]. The model solves the momentum and thermodynamic ocean equations using a second order finite-volume flux scheme, which combines the advantages of finite-element methods for geometric flexibility and finite difference methods for computational efficiency. The most important feature of FVCOM adopted in this coupled model is its unstructured grids, which allows us to design varying and sufficiently fine resolutions to resolve the complex topography, embedded archipelago, internal straits/seas, and throughflows within the Maritime Continent. The model topography was interpolated from ETOPO2 data set.

The model domain was set from 85°E to 142°E and from 20°S to 30°N, covering the entire SCS, the Indonesian seas, and large sections of the western Pacific and eastern Indian Oceans (Figure 1). The resolution of RegCM3 was set to 60 km. The resolution of FVCOM varied from $\sim$5 km along the shelf break and in the straits, to $\sim$10 km along the coastlines, to $\sim$50 km over the Sunda shelf and deep areas of the SCS basin, and $\sim$200 km along the open boundaries. The coupled model was driven by the 6 h ERA-40 reanalysis (http://apps.ecmwf.int/datasets/) for the lateral boundary conditions of the atmospheric model and by the Simple Ocean Data Assimilation (SODA, version 2.2.4) [*Carton et al*., 2000a,2000b] reanalysis (http://www.atmos.umd.edu/~ocean/) for the lateral boundary conditions of the ocean model. Surface fluxes were exchanged every 3 h between RegCM3 and FVCOM through the coupler (OASIS3), which interpolates atmospheric-oceanic variables (winds, heat fluxes, freshwater flux, and SST) between the two model grids. For more detailed information about the coupled model, please refer to *Wei et al*. [2014a], who originally developed the coupled model, and *Wei et al*. [2014b], for a comprehensive validation in the SCS. Moreover, *Xu and Malanottte-Rizzoli* [2013] validated the Indonesian Throughflow (ITF) in the ocean-only component against in situ observations, and *Xue et al*. [2014] examined the local air-sea feedback mechanisms over the entire Maritime Continent using the fully coupled model.

2.2. Model Configurations for the Sensitivity Experiments

The sensitivity experiments in this study are based on the concept of a partial-coupling (P-C) method used widely in global fully coupled GCMs [*Wu et al*., 2003; *Zhong et al*., 2008; *Lu and Zhao*, 2012; *Luo et al*., 2014; *Ding et al*., 2014]; however, its applications in regional models has not been reported. In P-C experiments, one of atmospheric or oceanic variables is controlled in the coupled model, which allows for a partial air-sea coupling, and therefore the effect of the controlled variable can be determined by the difference between the fully coupled experiment (control run) and the P-C experiments. To apply this method into a regional coupled model to separate the surface and boundary forcing in the SCS, the model was specifically configured as follows. First, the fully coupled model was spun up from 1960 to 1970, with a SST relaxation to the SODA data, in order to obtain a realistic initial condition. The model was then restarted on 1 January 1970, by turning off the SST relaxation, and integrated forward until 1 January 2010, allowing a full air-sea coupling. The fully coupled simulation during 1970–2010 is referred as the control experiment (Exp. 1).

The temperature changes can be interpreted by the temperature budget equation

$$\underbrace{\frac{\partial T}{\partial t}}_{\mathrm{T}}=\underbrace{-\left(u\frac{\partial T}{\partial x}+v\frac{\partial T}{\partial y}+w\frac{\partial T}{\partial z}\right)}_{\mathrm{ADV}}+\underbrace{\frac{\partial}{\partial x}\left(A_h\frac{\partial T}{\partial x}\right)+\frac{\partial}{\partial y}\left(A_h\frac{\partial T}{\partial y}\right)}_{\mathrm{HDIF}}+\underbrace{\frac{\partial}{\partial z}\left(K_h\frac{\partial T}{\partial z}\right)}_{\mathrm{VDIF}}+\underbrace{\frac{Q}{h\rho_0 C_p}}_{\mathrm{HFX}}, \tag{1}$$

where the left-hand term is the rate of temperature changes; u, v, and w are ocean current velocities at x, y, and z directions, respectively; A_h and K_h are horizontal and vertical diffusivity; c_p is the specific heat of water, ρ_0 the water density, and h the mixed-layer depth. The terms on the right-hand side are advection (ADV), horizontal diffusion (HDIF), vertical mixing (VDIF), and heat flux (HFX), respectively. Note that the horizontal diffusion term (HDIF) is usually negligible compared to the other terms [*Uhlhorn and Shay*, 2013; *Wei et al*., 2014c]. The vertical mixing term (VDIF) is small within the surface mixed layer, but can be significantly important at subsurface, especially near the thermocline where the vertical temperature gradient is large.

Likewise, the horizontal momentum equations can be written as follows, if the bottom friction is neglected [*Knauss*, 1978]:

$$\frac{\partial u}{\partial t}=-\left(u\frac{\partial u}{\partial x}+v\frac{\partial u}{\partial y}+w\frac{\partial u}{\partial z}\right)+fv-\frac{1}{\rho_0}\frac{\partial p}{\partial x}+\frac{\partial \tau_x}{\partial z}, \tag{2}$$

$$\frac{\partial v}{\partial t}=-\left(u\frac{\partial v}{\partial x}+v\frac{\partial v}{\partial y}+w\frac{\partial v}{\partial z}\right)-fu-\frac{1}{\rho_0}\frac{\partial p}{\partial y}+\frac{\partial \tau_y}{\partial z}, \tag{3}$$

where u and v are eastward and northward current velocity, respectively; f is the Coriolis parameter; p is the pressure; and τ refers to the wind stress on the ocean surface for surface velocities and interfacial stress for subsurface velocities. If KE is defined as $(u^2+v^2)/2$, combining equations (2) and (3), the KE budget equation can be derived as follows [*Wei et al*., 2014c]:

$$\underbrace{\frac{\partial KE}{\partial t}}_{\mathrm{K}}=\underbrace{-\left(u\frac{\partial KE}{\partial x}+v\frac{\partial KE}{\partial y}+w\frac{\partial KE}{\partial z}\right)}_{\mathrm{ADV}}\underbrace{-\frac{1}{\rho_0}\left(u\frac{\partial p}{\partial x}+v\frac{\partial p}{\partial y}\right)}_{\mathrm{PWH}}+\underbrace{\left(u\frac{\partial \tau_x}{\partial z}+v\frac{\partial \tau_y}{\partial z}\right)}_{\mathrm{WND}}. \tag{4}$$

The left-hand term is the rate of KE changes. The right-hand terms are advection (ADV), pressure work by horizontal currents (PWH), and wind stress work (WND), respectively. The large-scale surface circulation in the SCS, driven mostly by the monsoon winds, can be represented by WND, and the Luzon Strait inflow is represented by ADV. Note that the PWH term reflects a geostrophic circulation when PWH = 0, and therefore it becomes important only for ageostrophic flows.

To separate the surface and boundary effects, a set of experiments were designed based on the control experiment (Exp. 1). In Exp. 2, the lateral oceanic boundary conditions were controlled; that is, a coupled simulation of the 1980s/1990s was carried out, in which the lateral boundary conditions of the ocean model (temperature, salinity, and transport) were specified using those from the control experiment of the 1970s. Since the Luzon Strait transport in this model is largely controlled by the flow transport specified at the ocean boundary, the effect of the Luzon Strait inflow can be determined by Exp. 1–2. In Exp. 3, the lateral atmospheric fluxes were controlled; that is, a coupled simulation of the 1980s/1990s was carried out, in which the lateral boundary fluxes (heat fluxes and winds) of the atmosphere model were specified using those from the control experiment of the 1970s. By doing so, for such a small SCS domain, the atmospheric surface fluxes of the domain interior are generally determined by the boundary conditions of the 1970s, and therefore the effect of the surface fluxes can be determined by Exp. 1–3. Specifically, taking SST and surface KE as examples, individual components can be derived as follows: the total SST/KE changes (TL_ΔSST/TL_ΔKE) were derived by Exp. 1 [(1980s + 1990s)/2] − Exp. 1 (1970s); the SST/KE changes induced by lateral boundary effects (BC_ΔSST/BC_ΔKE) by Exp. 1 (1980s/1990s) − Exp. 2 (1980s/1990s); and the SST/KE changes induced by the atmospheric surface flux effects (SF_ΔSST/SF_ΔKE) by Exp. 1 (1980s/1990s) − Exp. 3 (1980s/1990s). Note that since most of regional processes are boundary-control problems, in this study we only controlled model boundary conditions for the Exp. 2/3, and therefore the simulation of model interior is still fully coupled.

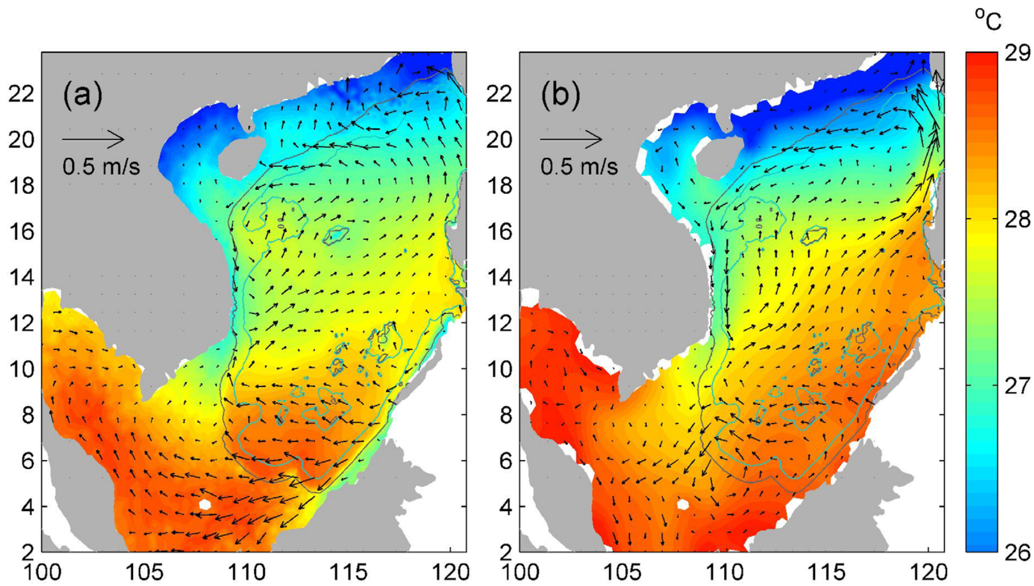

Figure 2. Comparison of the decadal-averaged (1970s–1990s) SST and surface velocity fields from the (a) coupled model and (b) SODA data. The black and green contours indicate the 200 and 1000 m isobaths, respectively.

3. Results

3.1 Simulations of SST and Circulations in the SCS

Figure 2 compares the decadal-averaged SST and surface flows (1970–2000) between the coupled model and SODA data. The coupled model generally reproduces the SODA velocity field, such as the cyclonic circulation in the northern SCS, representing a long-term ocean response to the Luzon Strait inflow and the monsoon winds. The cyclonic circulation brings cold water along the northern shelf of the SCS, turning southward along the east coast of the Vietnam and mixing with the central SCS water. On the shallow Sunda shelf (~40 m), away from the Luzon Strait, the model SST is almost homogenous and the circulation is mainly driven by monsoon winds, with westward surface flows. In contrast, the SODA produces a southward flow near the Karimata Strait. By comparing 10 m winds of ERA-40 used by SODA and the winds from the coupled model (not shown), the flow difference over the Sunda shelf is due to different wind forcing patterns.

Table 1. Comparison of the Model Transport With Previous Studies/Observations[a]

Straits	Transport (Sv)	References/Periods
Luzon Strait	−5.0	This study/1970–2010
	−6.0	*Tian et al.* [2006]/2005.10
	−4.4	*Metzger and Hurlburt* [1996]/1982–1983
	−5.2	*Hurlburt et al.* [2011]/2004–2009
	−5.6	*Xu and Malanotte-Rizzoli* [2013]/1960s
	−4.0	OFES/2004–2012
Karimata Strait	−1.2	This study/1970–2010
	−1 to −2	*Wyrtki* [1961]
	−0.58	*Gordon et al.* [2012]/2004–2011
	−1.4	*Xu and Malanotte-Rizzoli* [2013]/1960s
	−1.0	OFES/2004–2012
Mindoro Strait	−2.6	This study/1970–2010
	−2.4	*Qu and Song* [2009]/2004–2007
	−2.0	*Xu and Malanotte-Rizzoli* [2013]/1960s
	−3.1	*Metzger and Hurlburt* [1996]/1982–1983
	−1.6	OFES/2004–2012
Taiwan Strait	1.2	This study/1970–2010
	1.0	*Wyrtki* [1961]
	1.16–2.34	*Jan et al.* [2006]/1999–2001

[a]Positive/negative signs indicate northward/eastward and southward/westward flow, respectively.

Table 1 compares model strait transports with observations/reanalysis and previous numerical studies. It shows that our model reproduces reasonably well the total transport of in/outflows of the SCS. The model simulated transport through the Luzon Strait is ~5 Sv into the SCS. Although the observed Luzon Strait Transport is highly uncertain, varying from 0.5 to 10 Sv [*Qu et al.*, 1998; *Qu*, 2000; *Tian et al.*, 2006], our model estimate is consistent with results from previous model studies between 4.0 and 5.6 Sv [*Metzger and Hurlburt*, 1996; *Qu et al.*, 2006; *Tozuka et al.*, 2009; *Hurlburt et al.*, 2011; *Xu and Malanotte-Rizzoli*, 2013]. The outflows of the SCS are through three

Table 2. Correlation Coefficients Between ΔSST and Heat Flux, Wind Speed and Niño 3.4 Index[a]

	BC_ΔSST			SF_ΔSST		
Sites #	Heat Flux	Wind Speed	Niño3.4	Heat Flux	Wind Speed	Niño3.4
A	−0.37		−0.39	0.30		
B	−0.49	−0.45	–		−0.25	0.22
C	0.78	−0.27		0.62	−0.26	

[a]Empty cells indicate the correlation coefficient that is statistically insignificant.

major straits; the Karimata Strait (1.2 Sv), the Mindoro Strait (2.6 Sv), and the Taiwan Strait (1.2 Sv). The Mindoro Strait (up to 600 m depth) contributes largely to the SCS outflows, especially for the deep water, while the Karimata flow (average depth <40 m) is primarily driven by the seasonal reversing monsoons [*Wei et al*., 2016]. A comprehensive validation of the model simulations in the SCS and the Indonesian seas has been conducted by *Xu and Malanotte-Rizzoli* [2013] and *Wei et al*. [2014b].

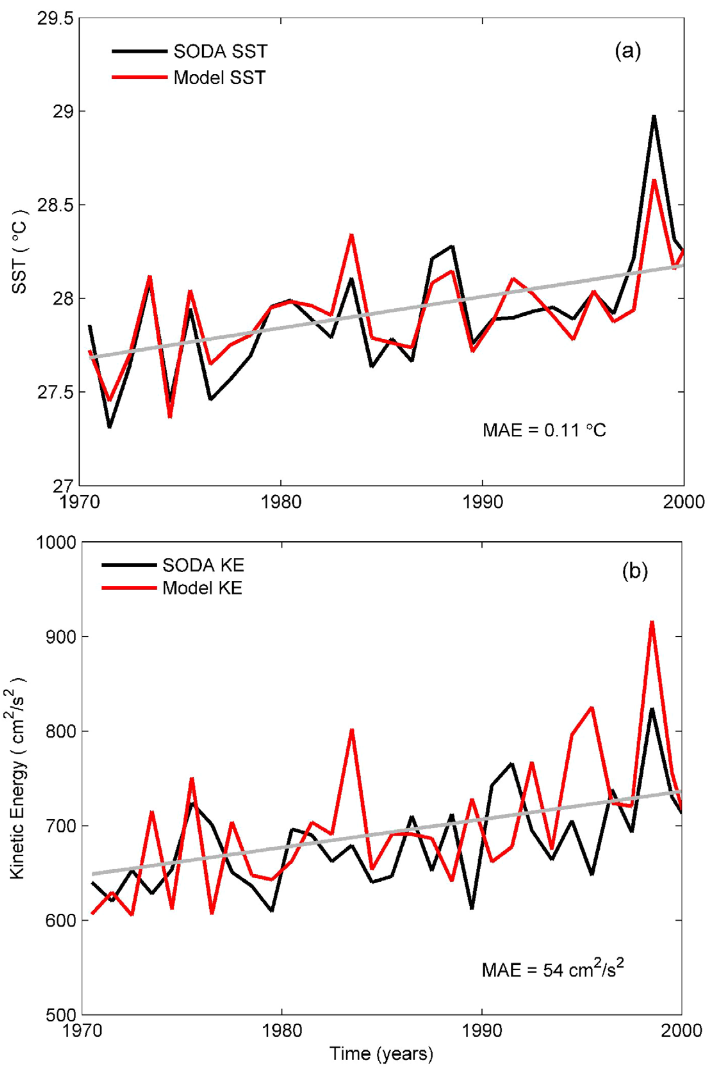

Figure 3. Comparison of the domain-averaged total (a) sea surface temperatures (SSTs) and (b) surface kinetic energy (KE) from the coupled model and SODA reanalysis, during 1970–2000. Their mean absolute errors (MAE) are given. The model SST and KE trends, calculated by linear regression at a significance level of 0.05, are superimposed.

As a part of the Indo-Pacific warm pool, SCS's SST warming has previously been recognized since late 1970s [*IPCC*, 2013; *Trenberth and Fasullo*, 2013; *Xu and Malanotte-Rizzoli*, 2013]. Figure 3 compares domain-averaged SST and KE between the coupled model and SODA reanalysis during 1970–2000. It appears that the coupled model is successful to reproduce the SODA SST warming trend and its interannual variability, with a mean-absolute-error (MAE) of 0.11°C and a correlation coefficient of 0.91. It also captures reasonably well the SODA KE variability, with a MAE of 54 cm^2/s^2 and a correlation coefficient of 0.62. Furthermore, the model results reveal that SST and KE in the SCS increase by about 0.5°C and 75 cm^2/s^2 from 1970 to 2000.

In this study, we are concerned with the decadal temperature and momentum changes from 1970 to 2000, during which period the climate shifted from a La Niña-like condition before 1976/1977 to an El Niño-like condition afterward. Figure 4 shows distributions of decadal SST changes during this transition period, that is [(1980s + 1990s)/2 – 1970s]. It appears that the coupled model also captures the SST anomaly pattern, compared with

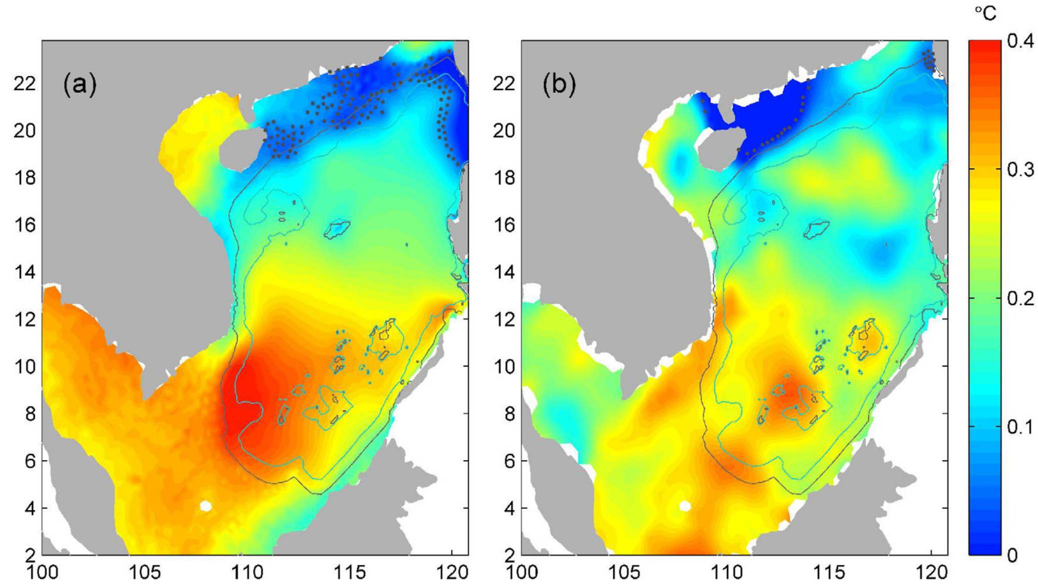

Figure 4. Horizontal patterns of decadal-averaged sea surface temperature (SST) changes derived from the (a) coupled model and (b) SODA reanalysis. The SST changes are defined as the SST differences between the 1980s/1990s and the 1970s (1980s/1990s – 1970s). The black and green contours indicate the 200 and 1000 m isobaths, respectively. The model grids are marked for insignificant SST changes, examined by *t*-test at a significance level of 0.05. Note that dark blue shading indicates the SST cooling area.

the SODA data, which is a data assimilation product. The SST warming mainly occurs in the southern part of the SCS, with a maximum warming of ~0.4°C. The warming in this region is far from the boundary exits (e.g., the Luzon Strait and the Karimata Strait) and thus can be intuitively attributed to the surface forcings (heat flux or winds). SST cooling occurs near the Luzon Strait, extending into the SCS along the continental shelf. This is apparently related to the cold-water inflow through the Luzon Strait. Note that dark blue area indicates the SST

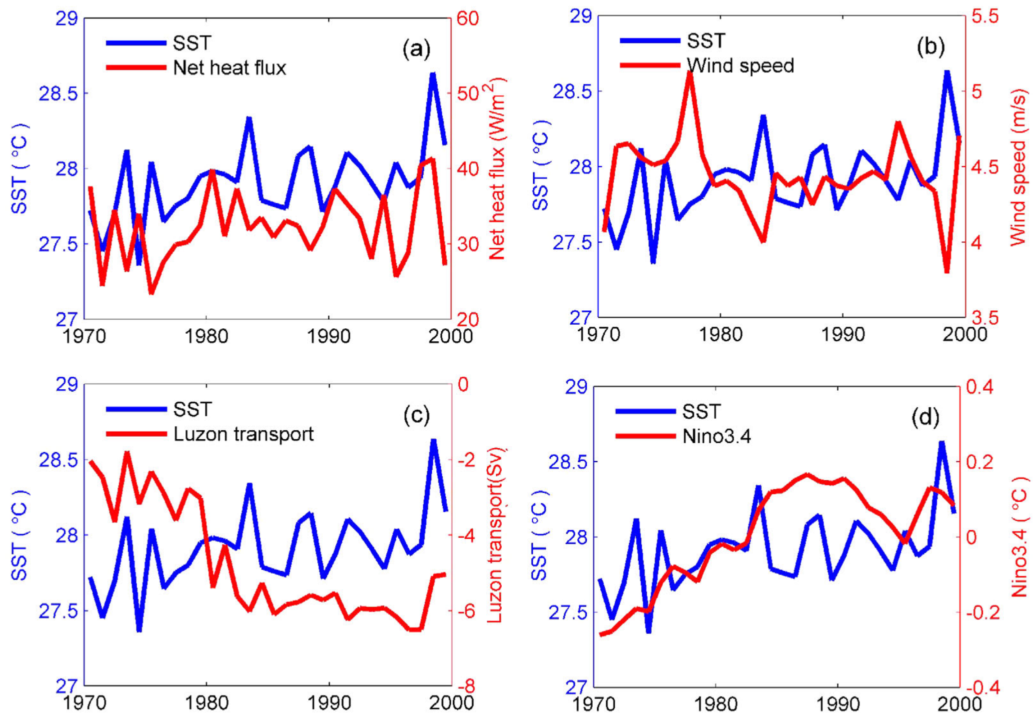

Figure 5. Comparisons between the sea surface temperatures (SSTs) and (a) net heat flux, (b) wind speed, (c) Luzon transport, and (d) Niño 3.4 index. To allow a comparison with the decadal SST trend, the monthly Niño 3.4 index was applied with a 10 year running mean.

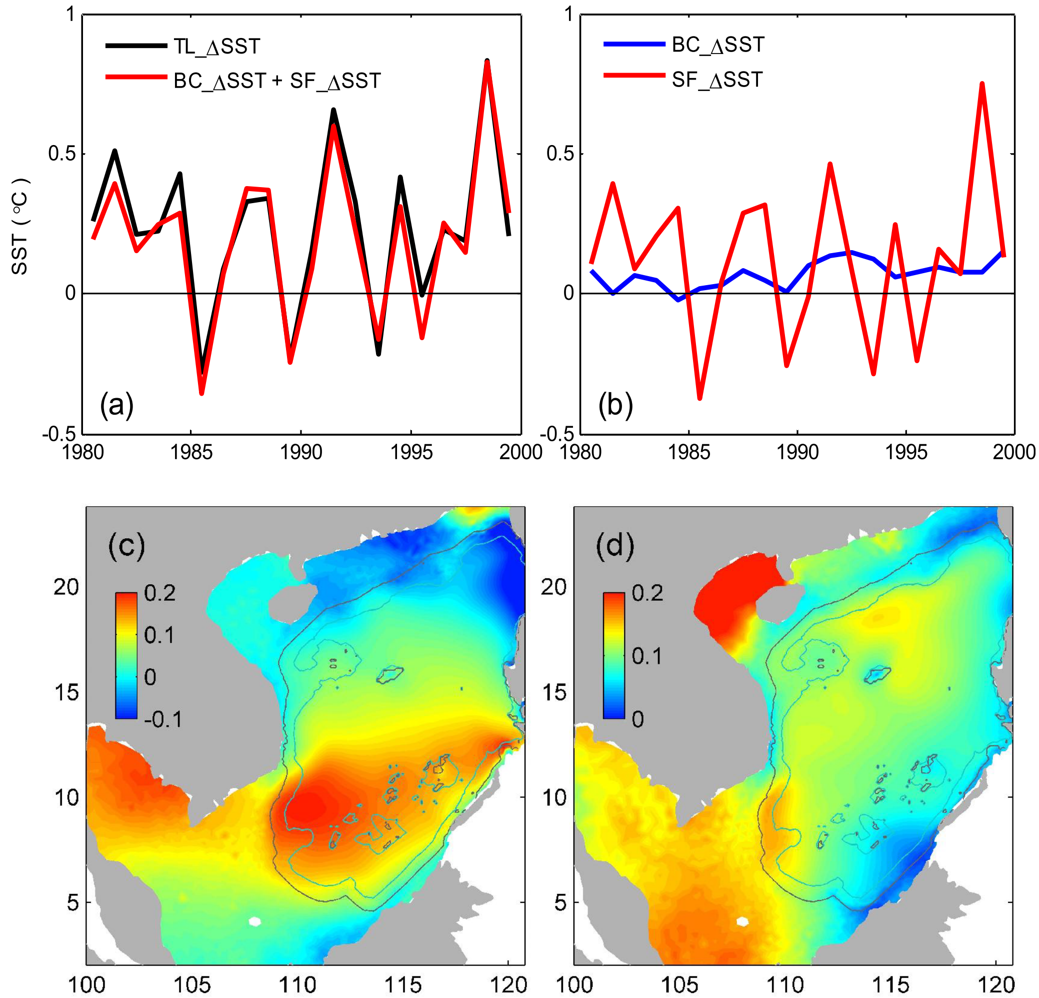

Figure 6. Comparisons of (a) the total SST changes (TL_ΔSST) and the combined SST changes due to boundary condition effects (BC_ΔSST) and surface flux effects (SF_ΔSST) and (b) the decomposed BC_ΔSST and SF_ΔSST. Horizontal patterns of the (c) BC_ΔSST and (d) SF_ΔSST components. The black and green contours indicate the 200 and 1000 m isobaths, respectively.

cooling (Figure 4a), while insignificant SST changes are marked by dots. The SODA SST generally shows a similar warming/cooling pattern, with some irregular patches.

To seek possible surface and boundary forcings responsible for the basin-scale SST changes, Figure 5 compares the SST variation with net heat flux, wind speed, Luzon Strait transport and Niño3.4 index. Among them, the net heat flux shows an evident increasing trend from 1970 to 2000, which is consistent with the concurrent SST warming trend. The Niño3.4 index, applied with a 10 year running mean, confirms that the global climate underwent a decadal transition period from a La Niña-like to an El Niño-like condition (Figure 5d). The ENSO variability is known to influence the Luzon Strait transport by modulating the interannual variability of the North Equatorial Currents (NEC). During an El Niño/La Niña-like condition, the Luzon intrusion increases/decreases as the NEC bifurcation moves northward/southward, which has been extensively investigated in previous studies [*Qiu and Lukas*, 1996; *Kim et al.*, 2004; *Qu et al.*, 1998, 2004; *Qiu and Chen*, 2010; *Chang and Oey*, 2012; *Zhai et al.*, 2014; *Chen and Wu*, 2015]. In accordance with this, our model is capable of simulating the decadal trend of the Luzon transport related to the climate phase shifting. The intrusion into the SCS is $\sim$2 Sv during 1970s and increases to $\sim$6 Sv during 1980–2000 (Figure 5c). One might readily expect that this enhanced cold-water inflow through the Luzon Strait could be responsible for the SST cooling in the northern SCS. On the other hand, the decadal SST warming trend seems to be unconnected to the decadal trend of the wind speed. Although their correlation coefficient of -0.21 is statistically insignificant, the winds apparently affect interannual SST changes (Figure 5b). For instance, the

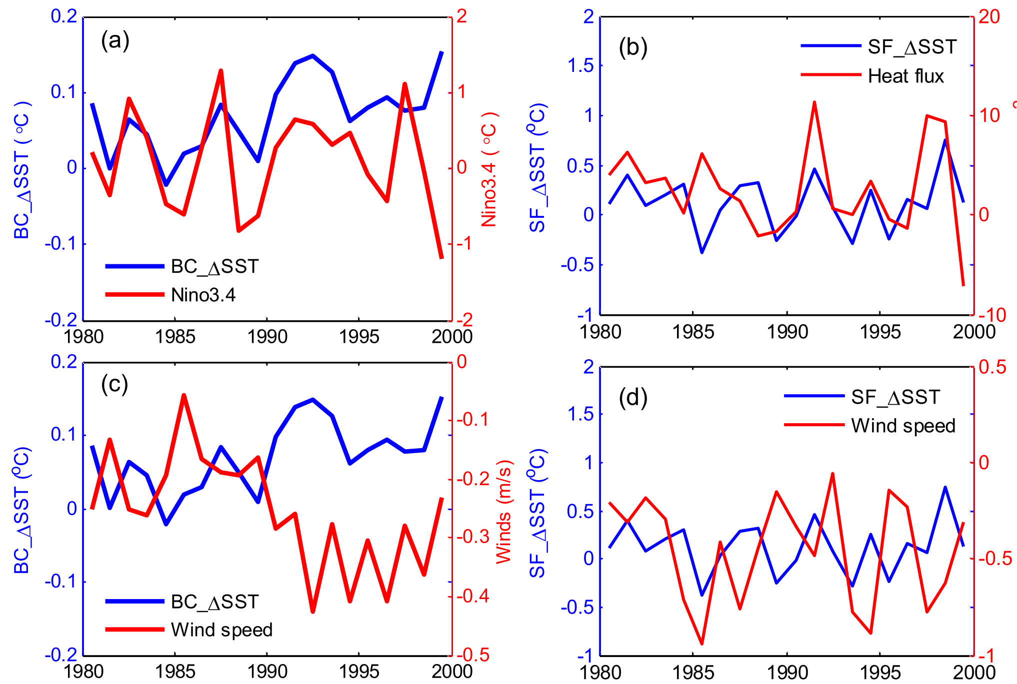

Figure 7. Comparisons between (a) BC_ΔSST and the Niño3.4 index; (b) SF_ΔSST and the associated net heat flux anomaly (Exp. 1–3); (c) BC_ΔSST and associated wind speed anomaly (Exp. 1–2); and (d) SF_ΔSST and associated wind anomaly (Exp. 1–3).

abrupt SST peaks in the years of 1983 and 1998 corresponds well to the weakening of winds during the strong 1982–1983 and 1997–1998 El Niño events.

3.2. Decomposition of SST Changes

According to the experiments described in section 2.2, the total SST changes (TL_ΔSST) can be decomposed into two components; those changes induced by the boundary effects (BC_ΔSST) and those induced by the surface effects (SF_ΔSST). Figure 6 displays temporal evolutions and spatial distributions of each component. It appears that the majority of the TL_ΔSST is represented by the combined BC_ΔSST and SF_ΔSST (Figure 6a), implying a successful linear decomposition. Between the two components, the SF_ΔSST is apparently the dominant one, contributing to 80% of the total SST changes, while the BC_ΔSST accounts only for ∼16% in amplitude (Figure 6b). The small misfit (∼4%) reflects the contributions from nonlinear processes and negligible terms, such as horizontal and vertical mixing (HDIF and VDIF). Spatially, the two components demonstrate different patterns in response to the surface and boundary forcings, respectively. The BC_ΔSST component shows remarkable cooling near the Luzon Strait, as well as notable warming over the central SCS basin along 10°N (Figure 6c). This result is in agreement with previous findings that, the northern SCS is influenced largely by the cold water intrusion from Pacific to the SCS through the Luzon Strait [*Qu et al.*, 2004]. In contrast, the SF_ΔSST shows a basin-wide warming in the SCS domain (Figure 6d).

To further understand the mechanism underlying the two components, Figure 7 compares the BC_ΔSST/SF_ΔSST with the Niño3.4 index, and associated heat flux/wind anomaly derived from the control and sensitivity experiments (Exp. 1–2/3). First, the interannual variation of the BC_ΔSST appears to be coherent with the Niño3.4 index (Figure 7a), with a correlation coefficient of 0.63, implying the effects of ENSO on the BC_ΔSST through the boundary. Second, the decadal BC_ΔSST warming trend seems to be coincident with weakened winds (Figure 7c), but uncorrelated with the surface heat flux (not shown). This implies that the major BC_ΔSST warming over the central SCS basin is most likely induced by the weakening of winds during the decadal El Niño-like period of 1980s–1990s. On the other hand, the SF_ΔSST component, with no significant decadal warming, generally follows the heat flux, with a correlation coefficient of 0.46 (Figure 7b). Recall that the maximum SF_ΔSST warming occurs over the Sunda shelf (Figure 6d, except for the Bay of Tonkin), where the heat flux-SST feedback is actively dominated [*Xue et al.*, 2014]. Meanwhile, the

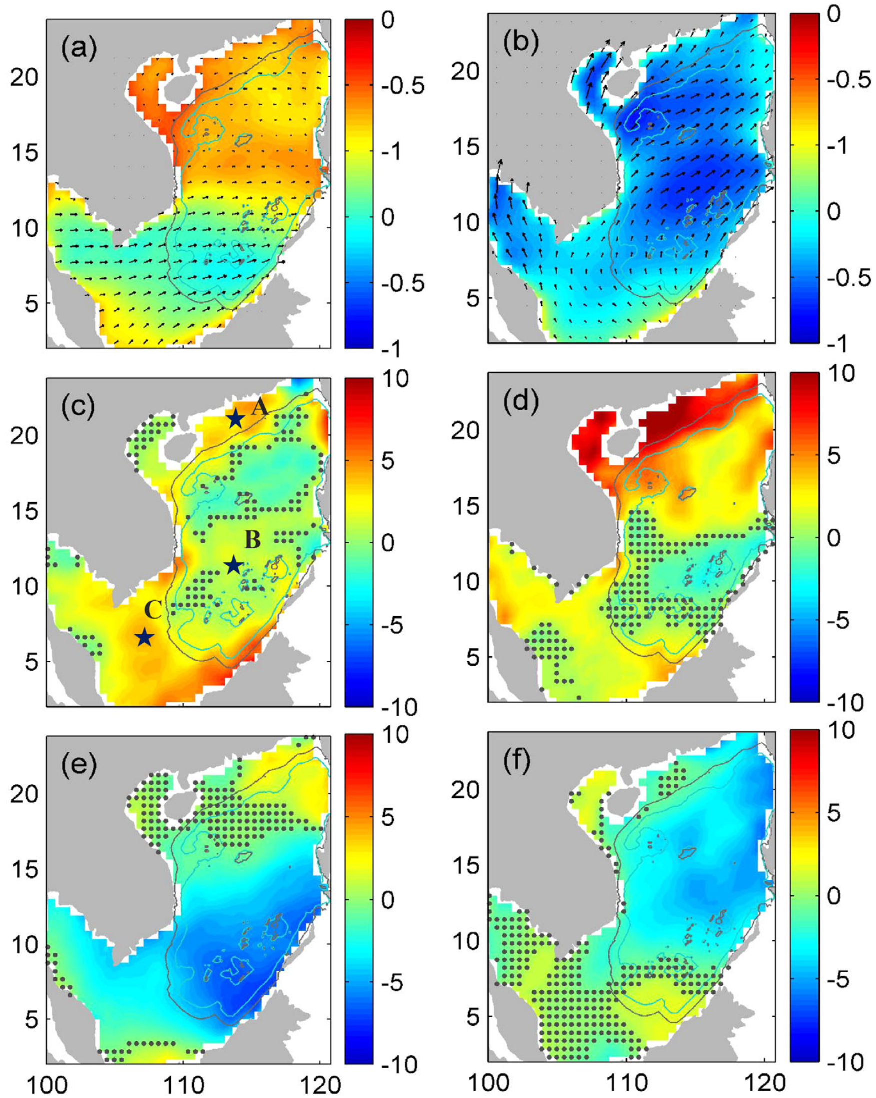

Figure 8. Distribution of anomalies for (a) wind speeds (shading) and wind fields (vectors), (c) net heat flux, and (e) latent heat flux derived from Exp. 1–2; and (b) wind speeds (shading) and wind fields (vectors), (d) net heat flux, and (f) latent heat flux from Exp. 1–3. The black and green contours indicate the 200 and 1000 m isobaths, respectively. Three typical locations described in the text are marked in Figure 8c.

SF_ΔSST is negatively correlated with the wind speed anomaly (Figure 7d), implying that the winds might be responsible to some extent for its maximum warming in the central SCS.

Figure 8 displays spatial distributions of the winds, net heat flux, and latent heat flux anomalies corresponding to the two components. For BC_ΔSST, the eastward wind vectors indicate the weakening of the local SCS winds during 1980–2000, which would reduce ocean evaporation and latent heat fluxes (Figure 8e); this is the major mechanism for the SST warming in the central SCS. The net heat flux anomalies are positive over shallow areas of the SCS (Figure 8c), due to an increase of its incoming solar radiation component (not shown), and are slightly negative in the central SCS, mainly due to the weakened latent heat flux (Figure 8e). Given that the net heat flux is positive in the northern SCS (Figure 8c), the ocean cooling there is caused by the cold water intrusion from the Pacific Ocean through the Luzon Strait (Figure 6c). For the warming of the SF_ΔSST, the basin-wide weakening of the winds (Figure 8b) and latent heat flux (Figure 8f) are apparently the major forcing, especially over the central SCS, however the net heat flux anomalies are negative (Figure 8d), mainly due to the decrease of the solar radiation flux (not shown). Correlation coefficients between ΔSST and heat flux, wind speed and Niño 3.4 index at three typical sites (marked in Figure 8c) are given in Table 2.

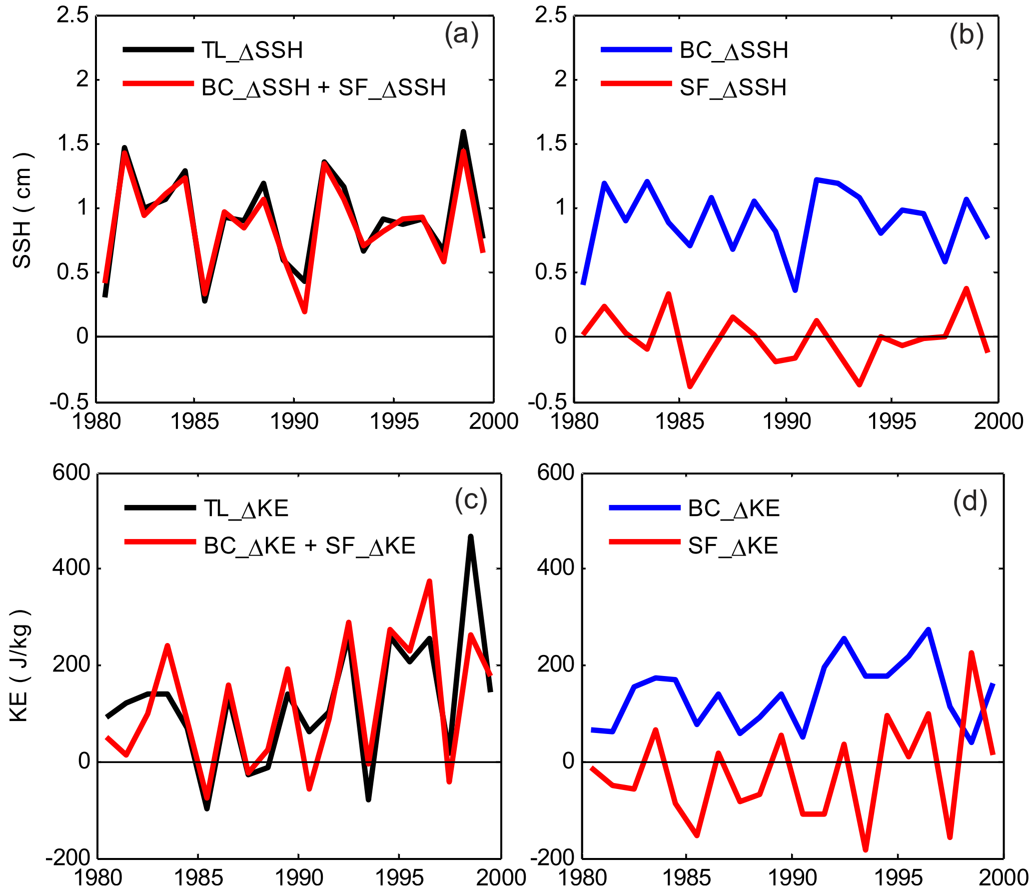

Figure 9. Comparisons between (a) TL_ΔSSH and the combined BC_ΔSSH and SF_ΔSSH; (b) the decomposed BC_ΔSSH and SF_ΔSSH; (c) TL_ΔKE and the combined BC_ΔKE) and SF_ΔKE; and (d) the decomposed BC_ΔKE and SF_ΔKE.

3.3. Decomposition of Surface KE Changes

The surface KE and sea surface height (SSH) were decomposed using the same procedure. Figure 9 shows the total SSH/KE changes (TL_ΔSSH/TL_ΔKE) and their associated components induced by the boundary effects (BC_ΔSSH/BC_ΔKE) and surface effects (SF_ΔSSH/SF_ΔKE). As expected, the TL_ΔSSH is primarily determined by the boundary component, BC_ ΔSSH (Figure 9b), as the SCS's dynamic heights are driven by the boundary forcings, instead of the surface fluxes. Accordingly, the total KE changes are mostly determined by the BC_ΔKE component too, which implies that the Luzon Strait transport plays a significantly important role in the SCS's circulations, through the boundary transport. Note that the misfit of the SSH is much smaller than that of the KE; this can be interpreted by the PWH term. According to the equations (2) and (3), PWH = 0 indicates a geostrophic flow $\left[u\frac{\partial p}{\partial x}+v\frac{\partial p}{\partial y}=u\left(\frac{\partial p}{\partial x}-fv\right)=0\right]$. The misfit of the SSH is smaller because the SSH generally reflects the geostrophic component (PWH = 0), while the surface KE includes both geostrophic and ageostrophic, wind-driven components.

Figure 10 shows the spatial distributions of the total SSH changes (TL_ΔSSH) superimposed by the surface velocity (TL_ΔUV), as well as the BC_ΔSSH/SF_ΔSSH components superimposed by BC_ΔUV/SF_ΔUV. As shown, the TL_ΔUV velocity in the northern SCS is generally driven by the TL_ΔSSH (geostrophic component dominated), while the TL_ΔUV in the southern SCS is apparently wind-driven (ageostrophic component dominated). The misfits between the total and decomposed velocities are plotted in Figure 10b; positive misfits generally occur in the regions of flow divergence (PWH > 0) and negative misfits are associated with flow convergence (PWH < 0). The boundary component (Figure 10c, BC_ ΔSSH/BC_ΔUV) is the dominant component, essentially similar to the total one, while the surface component (SF_ ΔSSH/SF_ΔUV) is significant only in the central SCS basin (Figure 10d). The cyclonic BC_ΔUV component in the northern SCS confirms the enhanced Luzon Strait transport during the El Niño-like period (1980–2000), while the

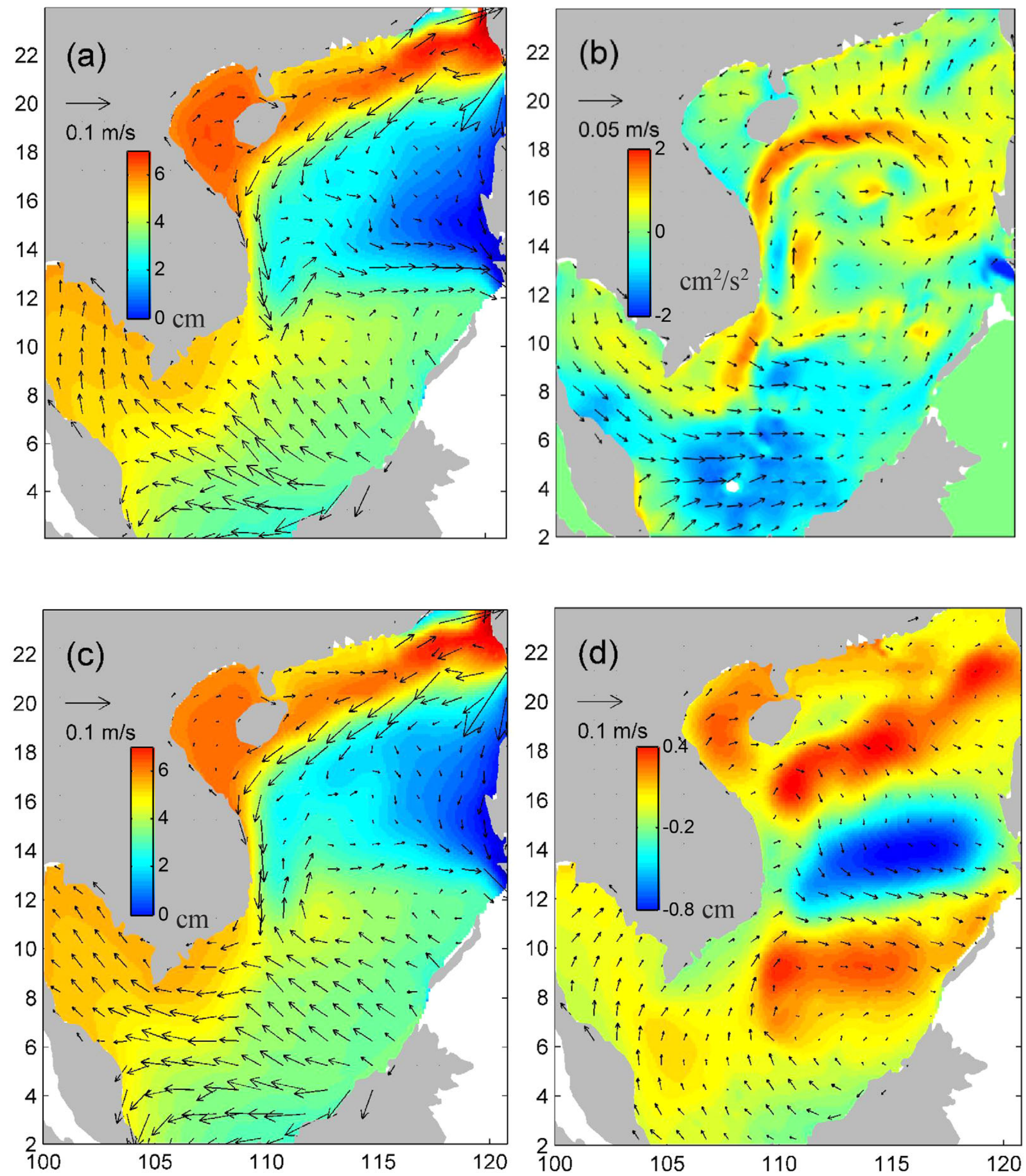

Figure 10. Decompositions of the total sea surface height (SSH) changes and surface current velocity: (a) Changes in the total SSH (TL_ΔSSH; shading) and changes in the total surface velocities (TL_ΔUV; vectors); (b) the misfits of surface kinetic energy (KE; shading) and velocity (vectors); (c) the changes in SSH (BC_ΔSSH; shading) and surface velocities (BC_ΔUV; vectors) due to boundary effects; and (d) the changes in SSH (SF_ΔSSH; shading) and surface velocities (SF_ΔUV; vectors) due to surface flux effects. Note that different color bars and vector scales are applied to each plot.

SF_ΔUV component represents an oceanic response to the weakened winds in the central SCS basin. Overall, these patterns are also consistent with the SST components, implying that the dynamic and thermal responses in the SCS are naturally interactive with each other.

Figure 11 displays the individual components for depth-averaged barotropic velocities (TL_ΔUVA/BC_ΔUVA/SF_ΔUVA) and their misfits. In contrast to the surface components, the changes in the barotropic velocity (TL_ΔUVA) demonstrate a persistent southward throughflow, inflowing from the Luzon Strait into the SCS and outflowing through the Karimata Strait. The TL_ΔUVA is nearly geostrophic, following the TL_ΔSSH isolines. Large misfits occur only near the east coast of Vietnam, the well-known upwelling zone, where the remarkable flow divergence is induced by the flow deflecting away from the coast. The BC_ΔUVA component is almost identical to TL_ΔUVA, while the SF_ΔUVA component is negligible, indicating that the boundary forcing plays a dominant role in driving the barotropic mode of the SCS circulations.

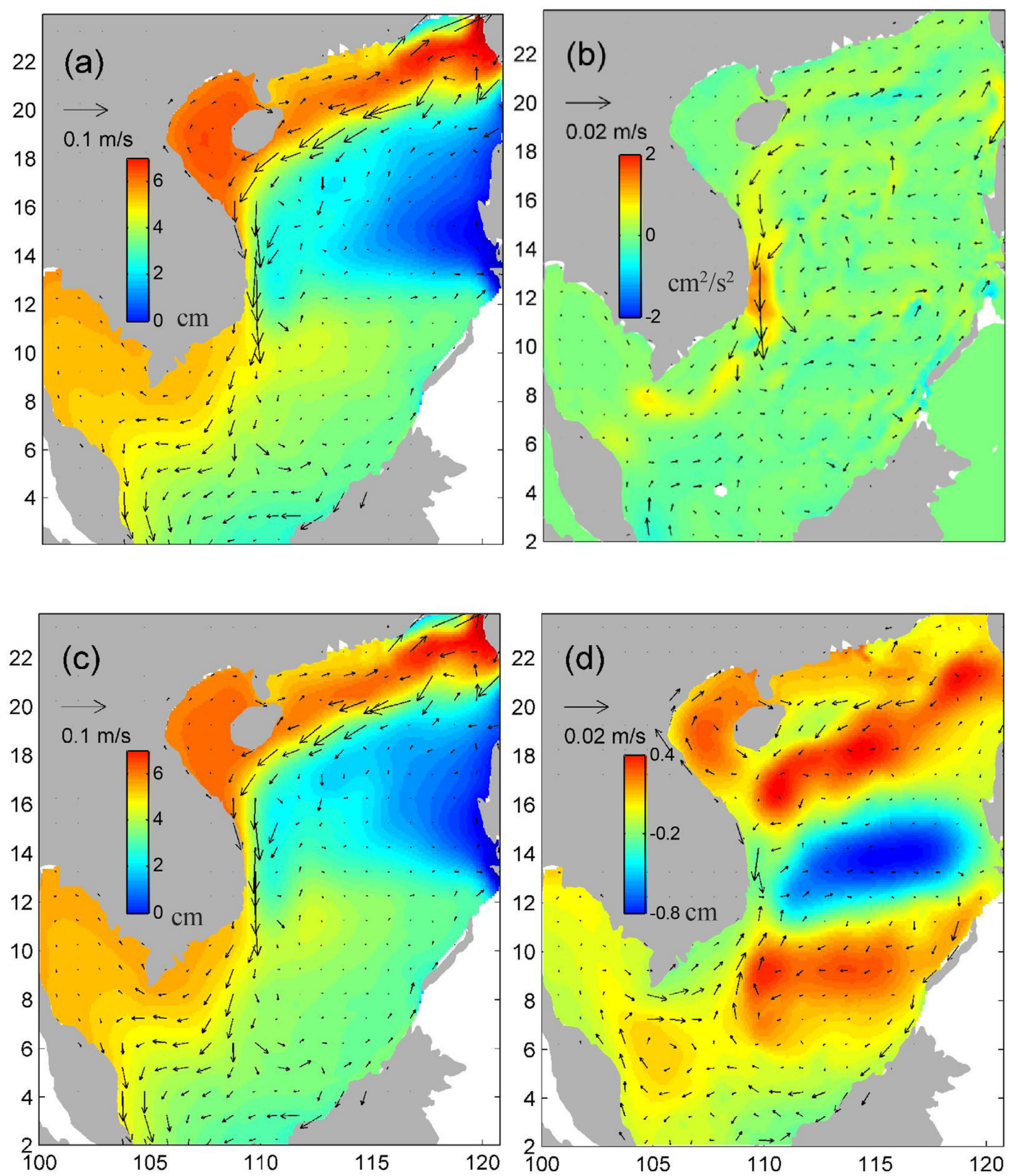

Figure 11. Same as the Figure 10, but for the decomposition of sea surface height (SSH) and barotropic depth-averaged velocity. Note that different color bars and vector scales are applied to each plot.

3.4. Subsurface Temperature and Momentum Structures

To examine vertical extensions that the surface and boundary forcings can affect the deep SCS basin, we further carried out decompositions for subsurface temperature and momentum components. Figure 12 shows the temporal evolution and spatial distributions of subsurface temperature and KE changes. A similar increasing trend of the subsurface temperature and KE can be found in the upper 500 m depth, but it becomes less prominent below 1000 m depth. The temperature pattern at 150 m depth indicate that the warming is located mainly in the southern SCS basin (Figure 12c). The increased KE is represented by a cyclonic throughflow into the SCS from the Luzon Strait and outflows to the Sulu Sea from the Mindoro Strait (Figure 12d). This flow pattern can penetrate down to 700 m depth (not shown), which is different from the surface throughflow through the Karimata Strait (Figure 11c). This deep throughflow separates the southern fast-warming water from the slow-warming water in the northern SCS, where the latter mixes with the cold-water inflow from the Luzon Strait.

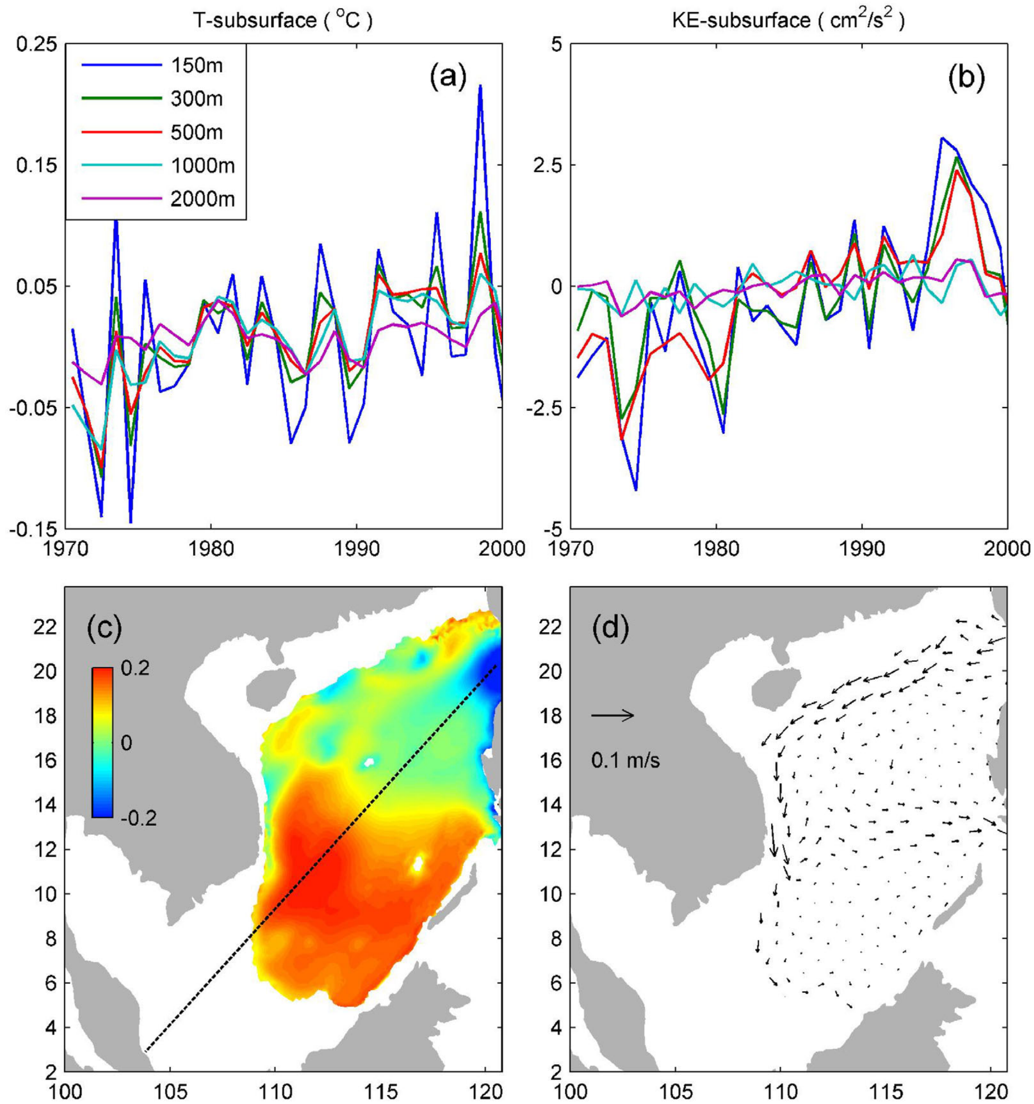

Figure 12. Evolution of subsurface changes for (a) temperature and (b) KE, and spatial distribution of the subsurface changes of (c) temperature and (d) velocity at 150 m depth. A cross-basin section is marked in Figure 12c.

Vertical profiles along a cross-basin section of the decomposed subsurface temperature components (BC_ΔSUB and SF_ΔSUB) and their misfits are plotted in Figure 13. It appears that the misfits are statistically insignificant near surface, but can be up to 0.15°C at about 300 m depth near the thermocline. On the other hand, the BC_ΔSUB shows remarkable warming in the southern SCS down to ~150 m depth, but cooling over the Sunda shelf and throughout the water column near the Luzon Strait (Figure 13c). This cooling extends towards the deep SCS basin below the surface warming. Insignificant temperature changes of the BC_ΔSUB generally occurs in a transition zone between the warming and cooling. In contrast, the SF_ΔSUB only affects the SCS thermal structure within upper 20 m (Figure 13d), below which depth the SF_ΔSUB are generally small or statistically insignificant. It is noteworthy that the surface temperatures changes induced by the surface and boundary forcing can penetrate down to ~150 m depth only, while they can be further transported downward into the deep SCS basin (~3000 m depth) by internal ocean mixing (Figure 13b).

4. Summary and Discussions

The SCS, the largest marginal sea located between the tropical Pacific and Indian Oceans, is a semi-enclosed basin, separated by island chains from the open oceans; as a result, its climate variability is

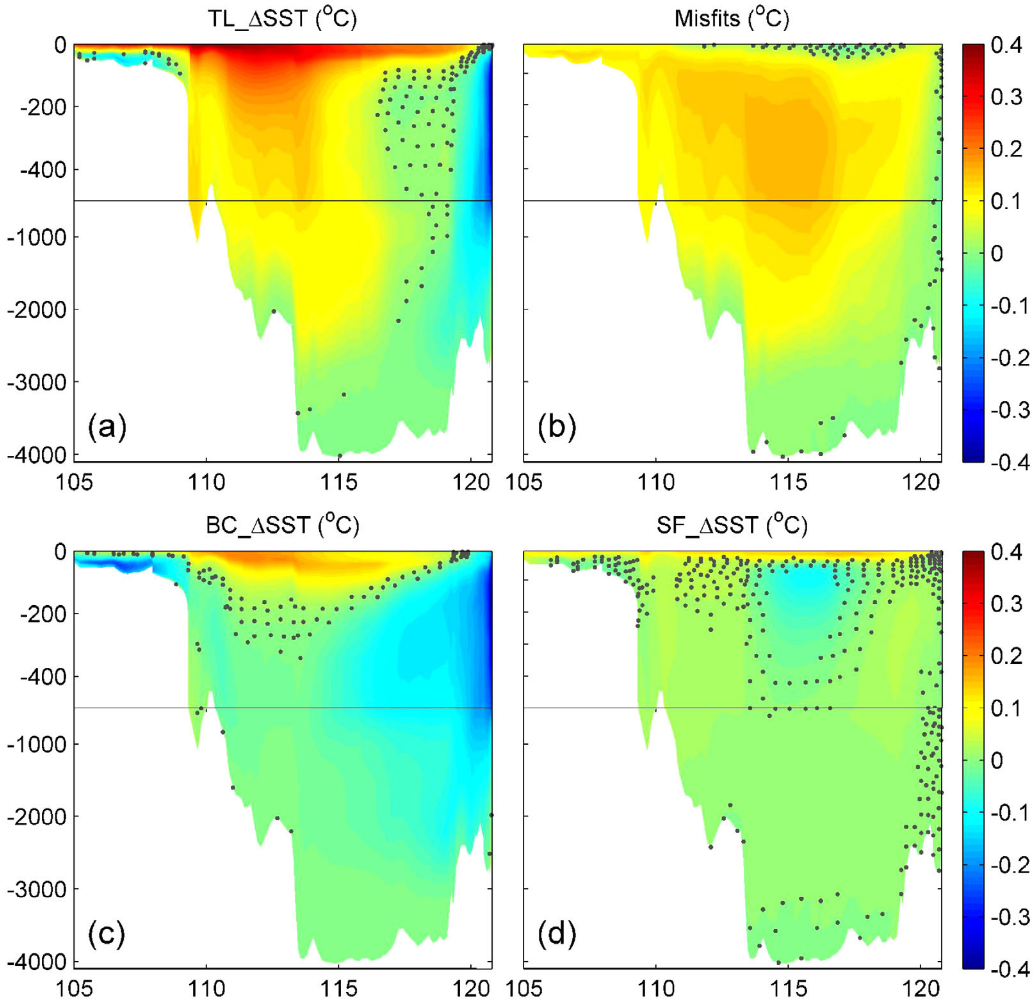

Figure 13. Cross-basin vertical sections of TL_ΔSST, BC_ΔSST, and SF_ΔSST components and their misfits. The section is marked in Figure 12c. Note that the upper 500 m is expanded to demonstrate the upper thermal structures. The model grids are marked for insignificant SST changes, examined by *t*-test at a significance level of 0.05.

determined jointly by both local air–sea interactions and remote forcings transferred into the SCS through oceanic and atmospheric passages, producing complex variability at multiple time and spatial scales. However, on the one hand, limited by its extremely complex geometry, topography and archipelago features, few existing regional coupled climate models have been able to fully resolve the two processes, which requires not only a large model domain to cover the entire Maritime Continent and adjacent oceans, but also sufficiently fine resolutions to resolve the island chains and straits. On the other hand, the two processes/forcings are naturally interactive in the SCS, and therefore difficult to separate from each other, which remains one of the major challenges for understanding the multiscale climate variability in the SCS.

Adopting an unstructured grid ocean model as the oceanic component, we have successfully developed a coupled regional climate model for the Maritime Continent, resolving the SCS with a minimal resolution of ~5 km along the shelf break and straits, covering large sections of the tropic Pacific and Indian Oceans and thus allowing remote forcings to transfer into the SCS through the model surface and lateral boundary effects. While we note that it is rather difficult to decipher the local and remote forcings from the coupled simulations, the effects of the remote forcing transferred into the SCS can be revealed from the model surface and boundary effects, separated by a set of sensitivity experiments using the coupled model.

In this study, the SCS's thermal and dynamic changes during 1970–2000 are decomposed into the two components: those induced by lateral boundary forcing and surface fluxes, respectively. The results showed that the two components together determined 96% of the total SST changes and 89% of the KE changes,

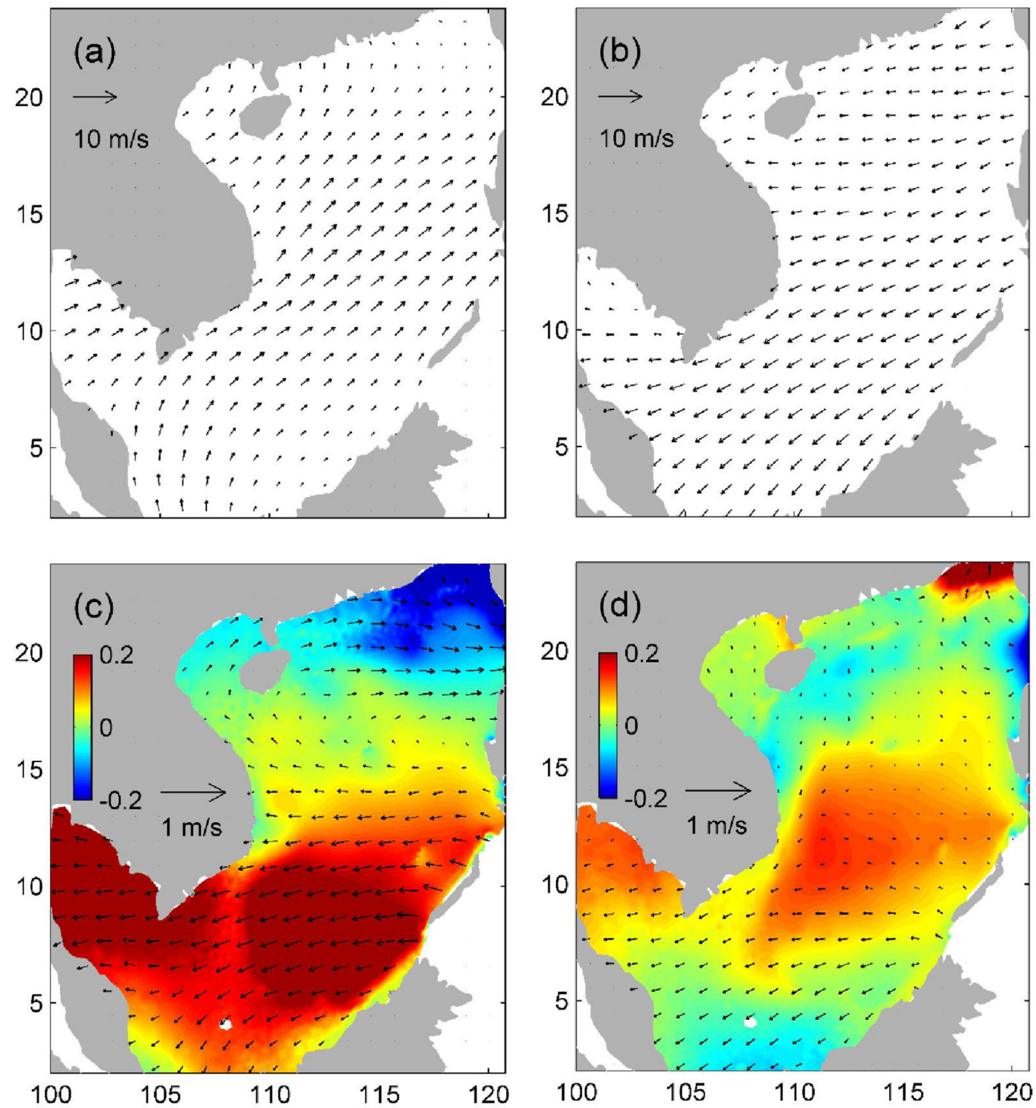

Figure 14. Coupled simulation of wind fields in the control experiment (Exp. 1) for (a) summer seasons (JJA) and (b) winter seasons (DJF); the wind anomaly (Exp. 1–2) for (c) summer seasons and (d) winter seasons. BC_ΔSSTs in summer and winter seasons are superimposed in Figures 14c and 14d for comparison.

implying a successful linear decomposition of the surface and boundary effects. The decomposed components demonstrated an evident increasing trend for both surface and subsurface temperature and momentum changes during 1970–2000. The increased subsurface SCS throughflow adopts a pathway from the Luzon Strait to the Mindoro Strait, different from the surface throughflow via the Luzon Strait to the Karimata Strait. This is attributed to the model flexible resolutions up to ~5 km, sufficiently fine enough to resolve the 40 km wide and 700 m deep Mindoro Strait. This deep SCS outflow plays a significantly important role to modulate the ITF variability [*Gordon et al.*, 2012; *Xu and Malanotte-Rizzoli*, 2013; *Wei et al.*, 2016].

Previous studies indicated that the air-sea coupling relationship in the SCS can be divided into a contrasting north-south pattern [*Xu and Malanotte-Rizzoli*, 2013] and a sandwich structure [*Wang et al.*, 2006c; *Wei et al.*, 2014b]. In general, it is considered that the northern SCS is substantially influenced by the Pacific intrusion flows through the Luzon Strait [*Liu and Xie*, 1999; *Liu et al.*, 2001a]. The southern SCS, as a part of the Indo-Pacific warm pool, is more likely influenced by westward propagating ENSO signals along the oceanic and atmospheric bridges [*Klein et al.*, 1999]. This argument is supported by the decomposed components obtained from this study. In the northern SCS, the enhanced cold water inflows intrude into the SCS during the decadal El Niño-like period of 1980s–1990s through the Luzon Strait (the oceanic bridge), shown as the cooling in the boundary component BC_ΔSST (Figure 6c) and the cyclonic circulation in the BC_ΔKE component (Figure 10c). In the central SCS basin, the weakening of winds favors the overall SST warming (atmospheric bridge), revealed by the SF_ΔSST (Figure 6d). Over the Sunda shelf, which is far from the exits and straits, the local air-sea interactions are dominated. Different from the previous studies, this study also explicitly presents the horizontal and vertical extensions of the surface and boundary effects.

Both BC_ΔSST and SF_ΔSST components indicate that winds play a significantly important role in the central SCS to determine SST variability through the Wind-Evaporation-SST (WES) mechanism [*Xie and Philander*, 1994; *Xie*, 1999], while the heat fluxes are more active over the continental shelf, where shallow waters favor the heat flux-SST feedback. The cold-water intrusion from the Luzon Strait leads to a northeastward SST gradient, and thus a southwestward wind anomaly is originated. Due to Coriolis force, this southwestward wind deviates to the west and weakens the summer monsoons (Figures 14a and 14c). Thus the evaporation of the central SCS basin is weakened, thereby warming up ocean SST and further enhancing the northeastward SST gradients. On the other hand, the temperature gradient crossing the northern SCS and mainland China results in an eastward wind anomaly, thereby accelerating the summer monsoons and further cooling down the SST near the Luzon Strait. In contrast, this WES feedback becomes less prominent in winter, for which the wind anomaly accelerates the northeastly winter monsoons (Figures 14b and 14d).

Acknowledgments
This study was supported by the National Natural Science Foundation of China (41476008 and 41576018), the Major State Basic Research Development Program (2015CB452805), the Strategic Priority Research Program of the Chinese Academy of Sciences (XDA11010303), and the Singapore-MIT Alliance for Research and Technology under the CANSAM program. We thank the European Centre for Medium-Range Weather Forecasts (ECMWF, http://apps.ecmwf.int/datasets/) for providing the ERA-40 reanalysis for the atmospheric boundary conditions, the Simple Ocean Data Assimilation (SODA) reanalysis (http://www.atmos.umd.edu/~ocean/) for the oceanic boundary conditions, and the Climate Prediction Center of the National Oceanographic and Atmospheric Administration (NOAA, http://www.cpc.ncep.noaa.gov/) for the Niño3.4 index data. All model data used in this study are outputted from our FVCOM-RegCM3 coupled model, and are available at http://www.atmos.pku.edu.cn/MC_coupled_model/.

References

Abraham, J. P., et al. (2013), A review of global ocean temperature observations: Implications for ocean heat content estimates and climate change, *Rev. Geophys.*, *51*, 450–483, doi:10.1002/rog.20022.
Balmaseda, M. A., K. E. Trenberth, and E. Källén (2013), Distinctive climate signals in reanalysis of global ocean heat content, *Geophys. Res. Lett.*, *40*, 1754–1759, doi:10.1002/grl.50382.
Carton, J. A., G. Chepurin, X. Cao, and B. S. Giese (2000a), A simple ocean data assimilation analysis of the global upper ocean 1950-1995, Part 1: Methodology, *J. Phys. Oceanogr.*, *30*, 294–309.
Carton, J. A., G. Chepurin, and X. Cao (2000b), A simple ocean data assimilation analysis of the global upper ocean 1950-1995 Part 2: Results, *J. Phys. Oceanogr.*, *30*, 311–326.
Chang, Y. L., and L. Y. Oey (2012), The Philippines-Taiwan Oscillation: Monsoon-like interannual oscillation of the subtropical-tropical western North Pacific wind system and its impact on the ocean, *J. Clim.*, *25*, 1597–1618.
Chen, C.-T., and M.-H. Huang (1996), A mid-depth front separating the South China Sea water and the Philippine Sea water, *J. Oceanogr.*, *52*, 17–25, doi:10.1007/BF02236530.
Chen, J. M., C. P. Chang, and T. Li (2003a), Annual cycle of the South China Sea surface temperature using the NCEP/NCAR reanalysis, *J. Meteorol. Soc. Jpn.*, *81*(4), 879–884.
Chen, C., H. Liu, and R. C. Beardsley (2003b), An unstructured, finite-volume, three-dimensional, primitive equation ocean model: Application to coastal ocean and estuaries, *J. Atmos. Oceanic Technol.*, *20*, 159–186.
Chen, Z., and Wu, L. (2015), Seasonal variation of the Pacific South equatorial current bifurcation, *J. Phys. Oceanogr.*, *45*, 1757–1770.
Cheng, X.-H., S.-P. Xie, Y. Du, J. Wang, X. Chen, and J. Wang (2015), Interannual-to-decadal variability and trends of sea level in the South China Sea, *Clim. Dyn.*, *46*, 3113–3126.
Clement, A., and P. DiNezio (2014), The Tropical Pacific Ocean—Back in the driver's seat?, *Science*, *343*(6174), 976–978, doi:10.1126/science.1248115.
Ding, H., et al. (2014), The variability of the East Asian summer monsoon and its relationship to ENSO in a partially coupled climate model, *Clim. Dyn.*, *42*, 367–379.
Du, Y., and Qu, T. (2010), Three inflow pathways of the Indonesian throughflow as seen from the simple ocean data assimilation, *Dyn. Atmos. Oceans*, *50*, 233–256.
Easterling, D. R., and M. F. Wehner (2009), Is the climate warming or cooling?, *Geophys. Res. Lett.*, *36*, L08706, doi:10.1029/2009GL037810.
England, M. H., S. McGregor, P. Spence, G. A. Meehl, A. Timmermann, W. Cai, A. S. Gupta, M. J. McPhaden, A. Purich, and A. Santoso (2014), Recent intensification of wind-driven circulation in the Pacific and the ongoing warming hiatus, *Nat. Clim. Change*, *4*, 222–227, doi:10.1038/nclimate2106.
Fang, G., Y. Wang, Z. Wei, Y. Fang, F. Qiao, and X. Hu (2009), Interocean circulation and heat and freshwater budgets of the South China Sea based on a numerical model, *Dyn. Atmos. Oceans*, *47*, 55–72.
Gordon, A. L. (1986), Interocean exchange of thermocline water, *J. Geophys. Res.*, *91*, 5037–5046.
Gordon, A. L., B. A. Huber, E. J. Metzger, R. D. Susanto, H. E. Hurlburt, and T. R. Adi (2012), South China Sea throughflow impact on the Indonesian throughflow, *Geophys. Res. Lett.*, *39*, L11602, doi:10.1029/2012GL052021.
Grell, G. A., J. Dudhia, and D. R. Stauffer (1994), Description of the fifth generation Penn State/NCAR Mesoscale Model (MM5), *Tech. Rep. TN-398+STR*, Natl. Cent. for Atmos. Res., Boulder, Colo.
He, Z. Q., and R. G. Wu (2013), Coupled seasonal variability in the South China Sea, *J. Oceanogr.*, *69*, 57–69, doi:10.1007/s10872-012-0157-1.
Hurlburt, H., E. Metzger, J. Sprintall, S. Riedlinger, R. Arnone, and T. Shinoda (2011), Circulation in the philippine archipelago simulated by 1/12° and 1/25° global HYCOM and EAS NCOM, *Oceanography*, *24*, 1–20.
IPCC (2013), *Climate Change 2013: The Physical Science Basis. Contribution of Working Group I to the Fifth Assessment Report of the Intergovernmental Panel on Climate Change*, edited by T. F. Stocker et al., 1535 pp., Cambridge Univ. Press, Cambridge, U. K.
Jan, S., D. D. Shen, and H. M. Kuo (2006), Water mass and throughflow transport variability in the Taiwan Strait, *J. Geophys. Res.*, *111*, C12012, doi:10.1029/2006JC003656
Kiehl, J. T., J. J. Hack, G. B. Bonan, B. A. Boville, B. P. Breigleb, D. L. Williamson, and P. J. Rasch (1996), Description of the NCAR Community Climate Model (CCM3), *NCAR Tech. Note TN-420+STR*, Natl. Cent. for Atmos. Res., Boulder, Colo. [Available at http://www.cgd.ucar.edu/cms/ccm3/TN-420/.]

Kim, Y.-Y., T. Qu, T. Jensen, T. Miyama, H. Mitsudera, H. W. Kang, and A. Ishida (2004), Seasonal and interannual variations of the Norhter Equatorial Current bifurcation in a high-resolution OGCM, *J. Geophys. Res.*, *109*, C03040, doi:10.1029/2003JC002013.

Klein, S. A., B. J. Soden, and N.-C. Lau (1999), Remote sea surface temperature variations during ENSO: Evidence for a tropical atmospheric bridge, *J. Clim.*, *12*, 917–932.

Knauss, J. A. (1978), *Introduction to Physical Oceanography*, Prentice Hall, Englewood Cliffs, N. J.

Kosaka, Y., and S.-P. Xie (2013), Recent global-warming hiatus tied to equatorial Pacific surface cooling, *Nature*, *501*, 403–407.

Levitus, S., et al. (2009), Global ocean heat content 1955-2008 in light of recently revealed instrumentation problems, *Geophys. Res. Lett.*, *36*, L07608, doi:10.1029/2008GL037155.

Levitus, S., et al. (2012), World ocean heat content and thermosteric sea level change (0-2000 m) 1955-2010, *Geophys. Res. Lett.*, *39*, L10603, doi:10.1029/2012GL051106.

Liu, W. T., and X. S. Xie (1999), Space-based observations of the seasonal changes of South Asian monsoons and oceanic responses, *Geophys. Res. Lett.*, *26*(10), 1473–1476.

Lin, C.-Y., C.-R. Ho, Q. Zheng, N.-J. Kuo, and P. Chang (2011), Warm pool variability and heat flux change in the global oceans, *Global Planet. Change*, *77*, 26–33, doi:10.1016/j.gloplacha.2011.02.006.

Liu, Q. Y., H. J. Yang, and Z. Y. Liu (2001a), Seasonal feature of the Sverdrup circulation in the South China Sea, *Prog. Nat. Sci.*, *11*(3), 202–206.

Liu, Q. Y., D. Wang, and Q. Xie (2012), The South China Sea throughflow: Linkage with local monsoon system and impact on upper thermal structure of the ocean, *Chin. J. Oceanol. Limnol.*, *30*(6), 1001–1009.

Liu, Q.-Y., D. Wang, X. Wang, Y. Shu, Q. Xie, and J. Chen (2014), Thermal variations in the South China Sea associated with the eastern and central Pacific El Niño events and their mechanisms, *J. Geophys. Res. Oceans*, *119*, 8955–8972, doi:10.1002/2014JC010429.

Lin, Y. C., L.-Y. Oey, J. Wang, and K. K. Liu (2016), Rossby waves and eddies observed at a temperature mooring in northern South China Sea, *J. Phys. Oceangr.*, *46*, 517–535, doi:10.1175/JPO-D-15-0094.1.

Liu, Z.-Y., H.-J. Yang, and Q.-Y. Liu (2001b), Regional dynamics of seasonal variability in the South China Sea, *J. Phys. Oceanogr.*, *31*, 272–284.

Lu, J., and B. Zhao (2012), The role of oceanic feedback in the climate response to 342 doubling CO_2, *J. Clim.*, *25*, 7544–7563, doi:10.1175/JCLI-D-11-00712.1.

Luo, Y., J. Lu, F. Liu, and W. Liu (2014), Understanding the El Niño-like oceanic response in the tropical pacific to global warming, *Clim. Dyn.*, *45*, 1945–1964, doi:10.1007/s00382-014-2448-2.

Meehl, G. A., J. M. Arblaster, J. T. Fasullo, A. Hu, and K. E. Trenberth (2011), Model-based evidence of deep-ocean heat uptake during surface-temperature hiatus periods, *Nat. Clim. Change*, *1*, 360–364.

Metzger, E. J., and H. E. Hurlburt (1996), Coupled dynamics of the South China Sea, the Sulu Sea, and the Pacific Ocean, *J. Geophys. Res.*, *101*, 12,331–12,352.

Qiu, B., and S. Chen (2010), Interannual-to-decadal variability in the bifurcation of the North Equatorial Current off the Philippines, *J. Phys. Oceanogr.*, *40*, 2525–2538.

Qiu, B., and R. Lukas (1996), Seasonal and interannual variability of the North Equatorial Current, the Mindanao Current and the Kuroshio along the Pacific western boundary, *J. Geophys. Res.*, *101*, 12,315–12,330.

Qu, T. (2000), Upper-layer circulation in the South China Sea, *J. Phys. Oceanogr.*, *30*, 1450–1460.

Qu, T., and T. Song (2009), Mindoro Strait and Sibutu Passage transports estimated from satellite data, *Geophys. Res. Lett.*, *36*, L09601, doi:10.1029/2009GL037314.

Qu, T., H. Mistudera, and T. Yamagata (1998), On the western boundary currents in the Philippine Sea, *J. Geophs. Res.*, *103*, 7537–7548.

Qu, T., Y. Y. Kim, M. Yaremchuk, T. Tozuka, A. Ishida, and T. Yamagata (2004), Can Luzon Strait transport play a role in conveying the impact of ENSO to the South China Sea?, *J. Clim.*, *17*, 3644–3657.

Qu, T., Y. Du, and H. Sasaki (2006), South China Sea throughflow: A heat and freshwater conveyor, *Geophys. Res. Lett.*, *33*, L23617, doi:10.1029/2006GL028350.

Qu, T., Y. T. Song, and T. Ymagata (2009), An introduction to the South China Sea throughflow: Its dynamics, variability, and application for climate, *Dyn. Atmos. Oceans*, *47*, 3–14.

Tian, J., Q. Yang, X. Liang, D. Hu, F. Wang, and T. Qu (2006), The observation of Luzon strait transport, *Geophys. Res. Lett.*, *33*, L19607, doi:10.1029/2006GL026272.

Tozuka, T., T. Qu, Y. Masumoto, and T. Yamagata (2009), Impacts of the South China Sea throughflow on seasonal and interannual variations of the Indonesian Throughflow, *Dyn. Atmos. Oceans*, *47*, 73–85.

Trenberth, K. E., and J. T. Fasullo (2013), An apparent hiatus in global warming?, *Earth's Future*, *1*(1), 19–32, doi:10.1002/2013EF000165.

Uhlhorn, E. W., and L. K. Shay (2013), Loop current mixed layer energy response to Hurricane Lili (2002). Part II: Idealized numerical simulations, *J. Phys. Oceanogr.*, *43*, 1173–1192.

Wang, D., et al. (2006a), Interannual variability of the South China Sea throughflow inferred from wind data and an ocean data assimilation product, *Geophys. Res. Lett.*, *33*, L14605, doi:10.1029/2006GL026316.

Wang, C., W. Wang, D. Wang, and Q. Wang (2006b), Interannual variability of the South China Sea associated with El Niño, *J. Geophys. Res.*, *111*, C03023, doi:10.1029/2005JC003333.

Wang, G., W. Huang, and H. Wang (2006c), Study on the temporal and spatial variability of atmosphere-ocean flux over South China Sea with HOAPS data, *Acta Oceanol. Sin.*, *28*(4), 1–8.

Wei, J., P. Malanotte-Rizzoli, E. A. B. Eltahir, P. Xue, and D. Xu (2014a), Coupling of a regional atmospheric model (RegCM3) and a regional ocean model (FVCOM) over the Maritime Continent, *Clim. Dyn.*, *43*, 1575–1594, doi:10.1007/s00382-013-1983-6.

Wei, J., D. Wang, M. Li, and P. Rizzoli (2014b), Coupled seasonal and intraseasonal variability in the South China Sea, *Clim. Dyn.*, *44*(9), 2463–2477.

Wei, J., X. Liu, and D. Wang (2014c), Dynamic and thermal responses of the Kuroshio to typhoon Megi (2004), *Geophys. Res. Lett.*, *41*, 8495–8502, doi:10.1002/2014GL061706.

Wei, J. P. Malanotte-Rizzoli, M. T. Li, and D. X. Wang (2016), Opposite variability of Indonesian Throughflow and South China Sea Throughflow in the Sulawesi Sea, *J. Phys. Oceanogr.*, doi:10.1175/JPO-D-16-0132.1.

Wu, L., Z. Liu, R. Gallimore, R. Jacob, D. Lee, and Y. Zhong (2003), Pacific decadal variability: The tropical Pacific mode and the North Pacific mode, *J. Clim.*, *16*, 1101–1120.

Wu, R. G. (2010), Subseasonal variability during the South China Sea summer monsoon onset, *Clim. Dyn.*, *34*, 629–642, doi:10.1007/s00382-009-0679-4.

Wyrtki, K. (1961), Physical oceanography of the southeast Asian waters, Scientific results of marine investigations of the South China Sea and the Gulf of Thailand, *NAGA Rep. 2*, 195 pp., Scripps Inst. of Oceanogr., La Jolla, Calif.

Xie, S.-P. (1999), A dynamic ocean-atmosphere model of the tropical Atlantic decadal variability, *J. Clim.*, *12*, 64–70.

Xie, S.-P., and S. G. H. Philander (1994), A coupled ocean-atmosphere model of relevance to the ITCZ in the eastern Pacific, *Tellus, Ser. A*, *46*, 340–350.

Xu, D., and P. Malanotte-Rizzoli (2013), Seasonal variation of the upper layer of the South China Sea and the Indonesian Seas: An ocean model study, *Dyn. Atmos. Oceans*, *63*, 103–130, doi:10.1016/j.dynatmoce.2013.05.002.

Xu, F.-H., and L.-Y. Oey (2014), State analysis using the Local Ensemble Transform Kalman Filter (LETKF) and the three-layer circulation structure of the Luzon Strait and the South China Sea, *Ocean Dyn.*, *64*, 905–923, doi:10.1007/s10236-014-0720-y.

Xu, F. H., and L. Y. Oey (2015), Seasonal SSH variability of the Northern South China Sea, *J. Phys. Oceanogr.*, *45*, 1595–1609, doi:10.1175/JPO-D-14-0193.1.

Xue, P., P. Malanotte-Rizzoli, J. Wei, and E. Eltahir (2014), Local feedback mechanisms in a coupled ocean-atmosphere model of the shallow water region around the Maritime Continent, *J. Geophys. Res. Oceans*, *119*, 6933–6951, doi:10.1002/2013JC009700.

Zeng, L., and D. Wang (2009), Intraseasonal variability of latent-heat flux in the South China Sea, *Theor. Appl. Climatol.*, *97*, 53–64.

Zhai, F., Q. Wang, F. Wang, and D. Hu (2014), Decadal variations of Pacific North Equatorial Current bifurcation from multiple ocean products, *J. Geophys. Res. Oceans*, *119*, 1237–1256, doi:10.1002/2013JC009692.

Zhong, Y., Z. Liu, and R. Jacob (2008), Origin of pacific multi-decadal variability in community climate system model, version 3 (CCSM3): A combined statistical and dynamical assessment, *J. Clim.*, *21*, 114–133.